

Gravitational Gradients at Satellite Altitudes in Global Geophysical Studies

Pavel Novák · Robert Tenzer

Received: 24 January 2013 / Accepted: 17 June 2013 / Published online: 4 July 2013
© Springer Science+Business Media Dordrecht 2013

Abstract Due to the ESA's satellite mission GOCE launched in March 2009, gravitational gradients sampled along the orbital trajectory approximately 250 km above the Earth's surface have become available. Since 2010, gravitational gradients have routinely been applied in geodesy for the derivation of global Earth's gravitational models provided in terms of fully normalized coefficients in a spherical harmonic series representation of the Earth's gravitational potential. However, in geophysics, gravitational gradients observed by spaceborne instruments have still been applied relatively seldom. This contribution describes their possible geophysical applications in structural studies where gravitational gradients observed at satellite altitudes are compared with those derived by a spectral forward modeling technique using available global models of selected Earth's mass components as input data. In particular, GOCE gravitational gradients are interpreted in terms of a superposition principle of gravitation as combined gravitational effects generated by a homogeneous reference ellipsoid of revolution, mean topographic and ice mass density distributions, depth-dependent mass density contrasts within bathymetry and lateral mass density anomalies with sediments and crustal layers. Respective gravitational effects are one by one removed from gravitational gradients observed at approximately 250 km elevation above ground. Removing respective gravitational gradients from observed gravitational gradients gradually reveals problematic geographic areas with model deficiencies. For the full interpretation of observed gravitational gradients, deficiencies of CRUST2.0 must be corrected and effects of deeper laying mass anomalies not included in the study considered. These findings are confirmed by parameters describing spectral properties of the gravitational gradients. The methodology can be applied for validating Earth's gravitational models and for constraining crustal models in the development phase.

P. Novák (✉)
New Technologies for the Information Society (NTIS), Faculty of Applied Sciences,
University of West Bohemia, Univerzitní 22, 30614 Plzeň, Czech Republic
e-mail: panovak@kma.zcu.cz

R. Tenzer
School of Geodesy and Geomatics, Wuhan University, 129 Luoyu Road, Wuhan, China

Keywords Bathymetry · Crust · Earth interior · Forward modeling · Gravitational gradients · Sediments · Spherical harmonics · Topography

1 Introduction

The gravity field and steady-state ocean circulation experiment (GOCE) satellite was launched by the European Space Agency (ESA) in March 2009; more details on the GOCE mission can be found in, e.g., Floborghagen et al. (2011). Since September 2009, the mission has been providing time series of high-quality gravitational gradients sampled along near-polar orbits at the elevation of approximately 250 km above ground. Observed gradients have routinely been used in geodesy for estimating global static Earth's gravitational models (EGMs) with first releases presented during the ESA's Living Planet Symposium in Bergen at the turn of June and July 2010.

Geophysics has routinely applied anomalous or disturbing gravity in structural studies of the Earth (even of extraterrestrial bodies). However, geophysical applications of gravitational gradients observed by the low Earth orbiting satellite GOCE have still been relatively sparse, although mapping Earth interior processes was among its original science objectives. Several contributions in the field appeared just recently. Forward modeling of gravitational gradients generated by topographic masses was discussed, for example, by Álvarez et al. (2012) and Hirt et al. (2012). Crust thickness estimates based on GOCE observations were presented in studies by Mariani et al. (2013) and Reguzzoni and Sampietro (2012). These studies suggest globally distributed gravitational gradients at satellite altitudes can be used to probe subsurface mass density distributions in a joint analysis with available global models that describe mass density distributions within topography, bathymetry, continental ice sheets, sediments and crust. Gravitational gradients observed by the GOCE gradiometer and computed by forward modeling from available global topographic and crustal models can constrain models of the interior structure of the Earth's crust by taking the advantage of a 3-D behavior of the gravitational field represented by gravitational gradients. Fundamental parameters such as crustal thickness and crustal inhomogeneous density structures can then be inverted that in turn provide answers to the questions regarding, e.g., crust formation and thermal evolution of interior masses.

Combined analysis of anomalous (or disturbing) gravity data with global topographic and crustal models was attempted, for example, by Phillips and Lambeck (1980), Wiczorek (2007) and Tenzer et al. (2009). Similar studies have even been performed for some extraterrestrial bodies (namely the Moon, Venus and Mars) with Rummel (2005) and Huang and Wiczorek (2012) as two examples of such studies. In this contribution, we focus on gravitational gradients of the Earth's gravitational field observed by the spaceborne gradiometer on board GOCE that form the Marussi (gradiometric) tensor. These data will be analyzed in terms of gravitational gradients computed by forward modeling from global mass density distribution models that comprise of a homogeneous geocentric biaxial ellipsoid (Heiskanen and Moritz 1967, Sect. 2–7), topography (solid Earth's masses with an adopted mean mass density exterior to the geocentric ellipsoid), bathymetry (ocean water with a depth-dependent mass density contrast), continental ice sheets and interior masses comprising of sediments and crustal layer.

Although the GOCE gravitational gradients are freely available nowadays (for GOCE data products, see ESA 2010), our study relies on one of the latest EGMs based on GOCE data, namely the GOCO-03S model Mayer-Gürr et al. (2012). This model in terms of fully

normalized potential coefficients complete to degree and order 250 represents—after their synthesis—observed gravitational gradients at the satellite altitude. These values will be compared to gravitational gradients computed by a spectral forward modeling technique of the gravitational potential, e.g., Balmino (1973), Lachapelle (1976), Rapp (1981) and Sünkel (1986). This method was later modified and applied by Novák and Grafarend (2006) for the evaluation of gravitational gradients at satellite altitudes generated by topographic and atmospheric masses. Recently, Novák et al. (2013) applied this method also for the evaluation of gravitational gradients generated by subsurface mass density anomalies, namely by sediments and crustal layers. This method facilitates the uniform mathematical formalism of computing gravitational gradient corrections of mass density contrasts within the Earth’s inner density structures, which was developed by Tenzer et al. (2012). It utilizes the expression for the gravitational potential (and its higher-order directional derivatives) generated by an arbitrary volumetric mass layer with a variable depth and thickness while having laterally distributed vertical mass density variations.

Although the GOCE-based gravitational models are currently available up to degree 250, in this study, the actual resolution of all computed values is limited by degree 90 which is implied by the limited spatial resolution (2 arc-deg) of the CRUST2.0 model. For selected mass components, such as topography and sea water, the effective resolution could easily be extended to (and beyond) degree 250. However, to keep all the gravitational effects (signal components) consistent, the unique maximum degree 90 is applied concisely. Both the resolution and the accuracy of current crustal models are obviously insufficient for the validation or interpretation of latest EGMs based on GOCE observations.

In Sect. 2, forward modeling of gravitational gradients generated by a volumetric layer with a 3-D varying mass density distribution using the spectral approach will shortly be reviewed; Sect. 3 describes applied global topographic and crustal models; Sect. 4 validates the spectral formulas by an independent integral-based approach; Sect. 5 summarizes and interprets numerical results obtained by spectral forward modeling from available global topographic and crustal models; and Sect. 6 concludes the article by discussing possible future developments.

2 Gravitational Gradients of Volumetric Mass Layers

In the following, we shall assume the Earth’s crust consists of distinguished volumetric mass layers with specific mass density distributions. In particular, topography, bathymetry, continental ice sheets, sediments and crust layers are described in such a manner by available global models (such as ETOPO, SRTM and CRUST, see Sect. 3 for more details). In the following, the apparatus of spherical harmonics will be applied in connection with the geocentric spherical coordinate system defined in terms of the geocentric radius r , geocentric co-latitude $0 \leq \theta \leq \pi$ and longitude $0 \leq \lambda < 2\pi$.

Let us assume that functions describing geometry and mass density distribution within each layer can be expressed as a real square-integrable function f as follows (spherical harmonic synthesis—SHS):

$$f(\Omega) = \sum_{n,m} f_{nm} Y_{nm}(\Omega), \quad (1)$$

with the pair of angular coordinates—geocentric direction $\Omega = (\theta, \lambda)$ and spherical harmonics Y of degree n and order m . The abbreviated notation for the double summation is introduced and used throughout the article (first summation is limited by degree 90)

$$\sum_{n,m} = \sum_{n=0}^{90} \sum_{m=-n}^n .$$

Numerical coefficients f_{nm} in Eq. (1) are then defined (spherical harmonic analysis—SHA)

$$f_{nm} = \int_{\Theta} f(\Omega') Y_{nm}^*(\Omega') d\Omega', \quad n \leq 90, \tag{2}$$

with complex conjugates Y^* of the spherical harmonics, e.g., Arfken (1985, Sect. 12.8). The following abbreviated notation for surface integration over the full spatial angle Θ is used in the text:

$$\int_{\Theta} d\Omega' = \int_0^{2\pi} \int_0^{\pi} \sin \theta' d\theta' d\lambda' .$$

The functional model for the gravitational potential V is based on the Newtonian theory of gravitation. Applying the superposition principle of gravitation yields the gravitational potential generated by a closed volumetric mass layer in the form

$$V(r, \Omega) = G \int_{\Theta} \int_{r_i(\Omega')}^{r_e(\Omega')} \varrho(\xi, \Omega') \mathcal{L}^{-1}(r, \Omega, \xi, \Omega') \xi^2 d\xi d\Omega' . \tag{3}$$

In this equation, 2-D functions r_i and r_e describe two closed star-shaped mutually not crossing surfaces—interior (i) and exterior (e)—and bounding mass density distribution ρ and G is the (universal) gravitational constant. The inverse of the Euclidean distance \mathcal{L} in Eq. (3) can be expanded into a series of spherical harmonics (Heiskanen and Moritz 1967, Sect. 1.15) as follows:

$$\mathcal{L}^{-1}(r, \Omega, r', \Omega') = \frac{1}{r} \sum_{n,m} \left(\frac{r'}{r}\right)^n \frac{1}{2n+1} Y_{nm}(\Omega) Y_{nm}^*(\Omega'), \tag{4}$$

that originates in Legendre’s addition theorem.

The gravitational potential V , see Eq. (3), can be then computed if the mass density distribution function ϱ and the two closed bounding surfaces— r_i and r_e —are known. In the following, a general mass density distribution function will be modeled as follows (Tenzer et al. 2011):

$$\varrho(r, \Omega) = \sum_{j=0} \alpha_j(\Omega) r(\Omega)^j . \tag{5}$$

Numerical coefficients α_j can be determined by fitting the mass density model to available mass density distribution data with α_0 representing the reference mass density. Their numerical values for static atmospheric and sea water masses were given, e.g., by Novák (2010) and Tenzer et al. (2011). Numerical coefficients for sediment and crust mass density are taken from CRUST2.0, and for topography, a constant mass distribution function is assumed. Mass density contrasts defined as

$$\Delta\varrho(r, \Omega) = \rho_0 - \varrho(r, \Omega), \tag{6}$$

were used for sea water masses, ice sheets, sediments and crust masses with the mean crust mass density ρ_0 of $2,670 \text{ kg m}^{-3}$ (Hinze 2003). Using one reference density for all the masses considered in this study shall be replaced by a multilayer reference density model which has still to be developed. However, these investigations have to be linked to more reliable future crustal models such as CRUST1.0 (Pasyanos et al. 2012).

Geometry of the two bounding surfaces is then defined in terms of their vertical separation function H from the geocentric reference sphere of radius R , see Eq. (1),

$$r(\Omega) = R + H(\Omega) = R + \sum_{n,m} H_{nm} Y_{nm}(\Omega). \tag{7}$$

Numerical coefficients H_{nm} of the separation function H can be computed, see Eq. (2),

$$H_{nm} = \int_{\Theta} H(\Omega') Y_{nm}^*(\Omega') d\Omega', \tag{8}$$

from available global topographic models (such as ETOPO, SRTM or DTM).

As the background EGM is given in terms of normalized coefficients in spherical harmonic expansion of the gravitational potential and respective gravitational gradients are spectrally limited, spherical harmonic representation of the gravitational potential V associated with a specific volumetric mass layer is sought. Substituting Eqs. (4) and (5) into Eq. (3) yields the gravitational potential

$$V(r, \Omega) = G \sum_{n,m} \left(\frac{1}{r}\right)^{n+1} \frac{1}{2n+1} Y_{nm}(\Omega) \int_{\Theta} Y_{nm}^*(\Omega') d\Omega' \int_{r_i(\Omega')}^{r_e(\Omega')} \zeta^{n+2} \sum_{j=0} \alpha_j(\Omega') \zeta^j d\zeta. \tag{9}$$

The summation and integration in Eq. (9) can mutually be interchanged as long as the series is uniformly convergent, cf. Leibnitz’s integral rule, see, e.g., Moritz (1990). Since our evaluation points are located at the GOCE altitude, there is no problem to fulfill this requirement. Substituting for the radial integral in Eq. (9)

$$F(\Omega') = \sum_{j=0} \alpha_j(\Omega') \int_{r_i(\Omega')}^{r_e(\Omega')} \zeta^{j+n+2} d\zeta = \sum_{j=0} \alpha_j(\Omega') \left[\frac{\zeta^{j+n+3}}{j+n+3} \right]_{r_i(\Omega')}^{r_e(\Omega')}, \tag{10}$$

one gets a function that represents both mass density distribution (α_j) and geometry (r_i and r_e) of gravitating masses under consideration. Performing its global spherical harmonic analysis

$$F_{nm} = \int_{\Theta} F(\Omega') Y_{nm}^*(\Omega') d\Omega', \tag{11}$$

the gravitational potential can finally be synthesized as follows:

$$V(r, \Omega) = GR^2 \sum_{n,m} \left(\frac{R}{r}\right)^{n+1} \frac{4\pi}{2n+1} F_{nm} Y_{nm}(\Omega) = \frac{GM}{R} \sum_{n,m} \left(\frac{R}{r}\right)^{n+1} V_{nm} Y_{nm}(\Omega), \tag{12}$$

where harmonic coefficients of the gravitational potential V are rescaled to the geocentric gravitational constant GM of the spherical Earth with the homogeneous mass density distribution ρ

$$GM = \frac{4}{3}\pi\rho GR^3. \quad (13)$$

Maximum degree 90 of the spherical harmonic expansion in Eq. (12) corresponds to the angular resolution $\Delta\theta$ (2 arc-deg) of the function F .

Mathematical expressions for second-order directional derivatives of the gravitational potential depend on the coordinate frame. The GOCE gradiometer provides gravitational gradients that refer to the gradiometer reference frame (GRF) with x the roll axis, y the pitch axis and z the yaw axis of the GOCE satellite. In this particular coordinate system, components V_{xy} and V_{yz} are significantly less accurate (ESA 2010). GRF coordinates can conveniently be rotated to the local north-oriented frame (LNOF) that is used in this study (observed V_{xy} and V_{yz} must be replaced prior the rotation). The origin of LNOF coincides with the satellite's center of mass and the z axis points toward the center of mass of the Earth. The x axis points toward the rotational axis of the Earth and is orthogonal to the mean orbital plane. Finally, the y axis completes the orthogonal right-handed reference frame. In LNOF, components of the gravity gradient tensor are expressed as linear combinations of derivatives of the gravitational potential V in the geocentric spherical coordinate system, see "Appendix 1". Thus, they can easily be computed (synthesized) from any EGM.

The spherical harmonic representation of the gravitational gradients reads

$$\Gamma(r, \theta, \lambda) = \nabla \otimes \nabla V(r, \theta, \lambda) = \frac{GM}{R} \sum_{n,m} V_{nm} \mathbf{Z}_{nm}(r, \theta, \lambda), \quad (14)$$

with the tensor-valued harmonics

$$\mathbf{Z}_{nm}(r, \theta, \lambda) = \nabla \otimes \nabla \left(\frac{R}{r} \right)^{n+1} Y_{nm}(\theta, \lambda). \quad (15)$$

The symbol \otimes stands for the tensor (outer) product of two vectors. The transformation into the Cartesian form of the tensor reads

$$\Gamma(x, y, z) = \nabla \otimes \mathbf{J}^T \nabla V(r, \theta, \lambda) + \mathbf{J}^T \Gamma(r, \theta, \lambda) \mathbf{J}. \quad (16)$$

with the Jacobian \mathbf{J} of transformation between normalized spherical and Cartesian coordinate frames, see Eqs. (36)–(41) in "Appendix 1".

3 Global Gravitational, Topographic and Crustal Models

Global Earth's gravitational models derived from GOCE gravitational gradients are currently limited by maximum degree of 250 (International Centre for Global Earth Models - ICGEM) with low degree coefficients usually derived from GRACE (Tapley et al. 2004) and LAGEOS (Cohen and Smith 1985) data. In this article, the model GOCO-03S has been used as their typical representative.

Any gravitational parameter is reduced prior to its geophysical interpretation for the effect of the so-called normal (gravitational) field that is represented by a homogeneous

biaxial geocentric ellipsoid. The parameters of the Geodetic Reference System 1980 (GRS-80, see Moritz 2000) described according to the Somigliana–Pizetti theory allow for the evaluation of respective (normal) gravitational gradients in any point outside the reference ellipsoid (at an orbital elevation)

$$U(r, \theta) = \frac{GM}{r} \sum_n \left(\frac{a}{r}\right)^{2n} U_{2n} P_{2n}(\theta), \quad (17)$$

with the harmonic coefficients (Heiskanen and Moritz 1967, Sect. 2.9) for $n \leq 10$

$$U_{2n} = (-1)^{n+1} \frac{3e^n}{(2n+1)(2n+3)} \left(1 - n + 5n \frac{J_2}{e}\right). \quad (18)$$

Parameters a (major semi-axis of the reference ellipsoid), e (first numerical eccentricity of the reference ellipsoid) and J_2 (dynamic form factor of the normal gravitational field) are given by GRS-80. Respective (normal) gravitational gradients are then defined as follows:

$$\Gamma^N(r, \theta) = \nabla \otimes \nabla U(r, \theta). \quad (19)$$

Topographic masses are defined as solid Earth's masses outside the reference ellipsoid. For their representation, the global topographic model DTM2006 (Pavlis et al. 2007) released along with EGM08 (Pavlis et al. 2012) is used as it directly represents a spherical harmonic model with the global equiangular resolution of 5 arc-min. In connection with the reference ellipsoid, one gets the two bounding surfaces required for the evaluation of the topographic potential: r_i is the reference ellipsoid and r_e is the topographic surface. Obviously, over the oceans, the two surfaces coincide. The mean topographic mass density of $2,670 \text{ kg m}^{-3}$ is then used as the mass density function ρ . In case of bathymetry, the gravitational potential generated by the seawater can be computed similarly: r_i represents the ocean bottom and r_e is the reference ellipsoid. A radially varying (depth-dependent) mass density function ρ (Tenzer et al. 2012) and a respective mass density contrast, see Eq. (6), are applied. The very same approach was applied in case of the continental ice sheets. For this, we used the 5 arc-min continental ice-thickness data from the DTM2006 data sets derived from Kort and Matrikelstyrelsen ice-thickness data for Greenland (Ekholm 1996) and from the updated ice-thickness data for Antarctica assembled by the BEDMAP project (Lythe et al. 2001).

For the internal structure of the Earth's crust, the available global crustal model CRUST2.0 (Bassin et al. 2000) consists of the following global volumetric mass layers: (soft and hard) sediments and (upper, middle and lower) crusts. The model was compiled from seismic reflection data and detailed data of ice and sediment thickness. The angular resolution of the model is 2 arc-deg that is equivalent to maximum spherical harmonic degree 90. The model consists of bounding (internal and external) surfaces r and respective laterally varying volumetric mass density functions ρ . The application of the spectral approach is then rather straightforward: one can compute harmonic coefficients that correspond to the products of geometric and mass density information for each layer within the global crustal model, see Eq. (10). These coefficients are then used for the spherical harmonic synthesis of the respective gravitational potential by Eq. (12) and of its gravitational gradients by Eqs. (14) and (16), respectively.

From the above overview, it is obvious that measured data and available global models may have different properties (namely spatial resolutions) that can complicate their direct comparison. Gravitational gradients up to degree/order 90 were evaluated for the effect of

topography, bathymetry and continental ice sheets as the CRUST2.0 model allowed for the evaluation of gravitational gradients generated by the sediments and three crustal layers only up to the same spherical harmonic degree/order. One should keep this in mind when comparing numerical values of respective effects.

4 Validation of the Spectral Approach

In this section, results based on spectral formulas (derived in Sect. 2) will be compared to those based on classical Newtonian integrals. Only the radial component of the Marussi tensor will be considered. Spectral representation of the gradiometric tensor is based on Eqs. (12) and (14), respectively. Gravitational gradients based on volume integration then read, see Eq. (3),

$$\Gamma(r, \Omega) = G \int_{\Theta} \int_{r_i(\Omega')}^{r_e(\Omega')} \varrho(\xi, \Omega') \Lambda(r, \Omega, \xi, \Omega') \xi^2 d\xi d\Omega', \quad (20)$$

with the tensor-valued integral kernel

$$\Lambda(r, \Omega, \xi, \Omega') = \nabla \otimes \nabla \mathcal{L}^{-1}(r, \Omega, \xi, \Omega'). \quad (21)$$

The radial component of the gradiometric tensor for a constant mass density function reads

$$\Gamma_{rr}(r, \Omega) = G\rho \int_{\Theta} \int_{r_i(\Omega')}^{r_e(\Omega')} D_r^2 \mathcal{L}^{-1}(r, \Omega, \xi, \Omega') \xi^2 d\xi d\Omega' = \frac{G\rho}{r^2} \int_{\Theta} I(r, \Omega, r_i, r_e, \Omega') d\Omega', \quad (22)$$

where D_r is the radial derivative. The integrand I in the surface integration can be evaluated analytically, see (Wild and Heck 2004, Eq. 3) and “Appendix 2”.

The two approaches were applied for the evaluation of the radial topographic gradient. In the case of the spectral approach, DTM2006 coefficients up to degree and order 2160 were used. For global numerical integration, a global grid of 5 arc-min mean elevations consistent with the DTM2006 model represented the input data (discrete representation of the function r_e). Values of the radial topographic gradient were computed over the parallel of 20 arc-deg south crossing partially the Pacific Ocean and the Andes (crossing the coastline of Chile close to the port city of Iquique) where large values of the topographic gradient occur. The parallel arc is 40 arc-deg long and values of the radial topographic gradient were computed with the step of 15 arc-min. Numerical values are plotted in Fig. 1 that shows the radial topographic gradient computed by the spectral approach (SHS/SHA), global integration (integration) and their respective differences (magnified by two orders of magnitude). Thus, over the parallel arc 161 values were computed ranging from -0.92 to 5.77 E (Eötvös = 10^{-9} s $^{-2}$). The standard deviation of the differences is 0.001 E, which means that the two methods provide comparable results.

Numerical tests were also performed by comparing values based on the spectral approach described in this article with values derived from the KIT model (Grombein et al. 2010). The KIT (Karlsruhe Institute of Technology) model contains spherical harmonic coefficients derived by spherical harmonic analysis of combined topographic, bathymetric and ice mass gravitational effects. Thus, the combined gravitational gradients of these three

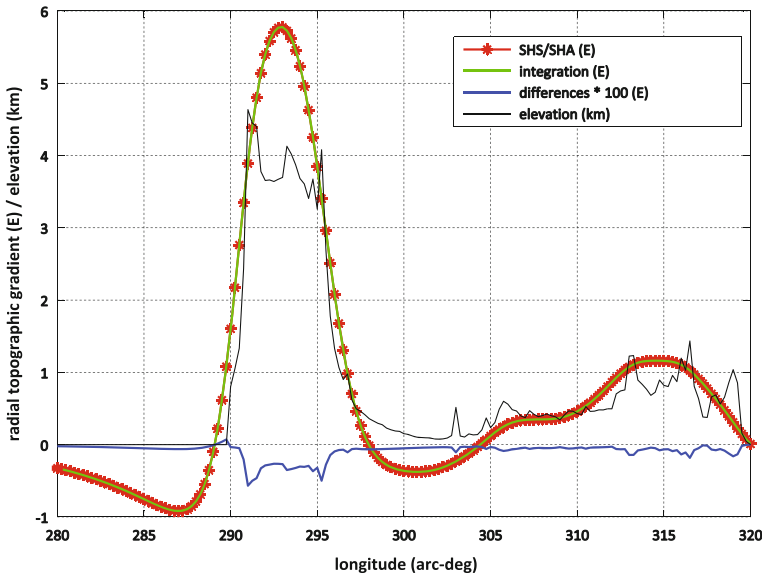


Fig. 1 Topographic gradient Γ'_{zz} : spectral approach (SHS/SHA) versus integration

masses can be synthesized at the satellite altitude. Gravitational gradients generated by topography, bathymetry and continental ice sheets computed with the spectral formulas formulated above had to be combined in one gravitational gradient. Figure 2 shows values of the radial gravitational gradient derived from the KIT model (KIT), respective values computed by the spectral approach combining the radial gravitational gradients of the three mass components (SHS/SHA) and their differences. The differences remain below 0.01 E over the parallel arc. The values match quite well considering the different approaches used for their evaluation: 1—masses are represented by tesseroids per each grid element, gravitational effects are computed by integration, and their respective spherical harmonic coefficients are derived by spherical harmonic analysis (KIT) versus 2—masses are represented by a continuous volumetric layer, spherical harmonic coefficients of functions defining their geometry and mass density distribution are derived by spherical harmonic analysis, and respective gravitational effects are finally evaluated by spherical harmonic synthesis (SHS/SHA).

5 Results and Their Interpretation

Numerical values of the gravitational gradients synthesized from GOCO-03S are compared to their respective values generated by the spectral approach described in Sect. 2 and by using input global data sets described in Sect. 3. In order to make the EGM-based gravitational gradients comparable to those derived by forward modeling, one defines first the disturbing (note the difference of the two adjectives “anomalous” and “disturbing” in this context) gravitational gradients

$$\delta\Gamma(r, \theta, \lambda) = \Gamma(r, \theta, \lambda) - \Gamma^N(r, \theta). \quad (23)$$

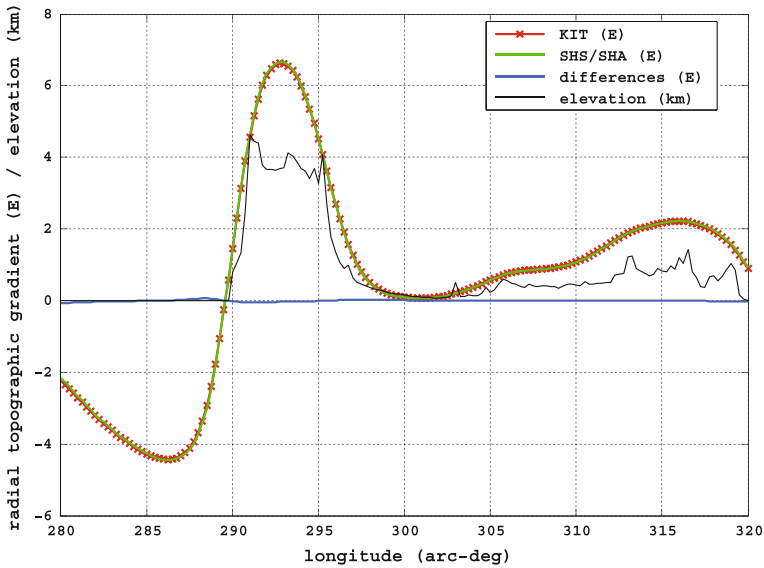


Fig. 2 Combined gradient Γ_{zz}^{r+b+i} : KIT-based results versus spectral approach (SHS/SHA)

Values of the three diagonal elements of the Marussi disturbing gravity gradient tensor in LNOF are shown in Fig. 3 produced by using GMT (Wessel and Smith 1991). These values represent counterparts to the components of the disturbing gravity vector $\delta\mathbf{g}$ often used in geodesy and geophysics.

Values of the disturbing gravitational gradients $\delta\Gamma$ in Eq. (23) correspond to 1—all masses external to the reference ellipsoid GRS-80, and 2—all mass density anomalies within the reference ellipsoid taken relatively to the adopted constant (mean) mass density of the reference ellipsoid (so-called mass density contrasts). External masses outside the reference ellipsoid consist of the atmosphere, topography and continental ice (neglecting the effect of water in large lakes and oceans). As numerical values of the gravitational gradients generated by global atmospheric masses are much smaller compared to other gravitational gradient corrections, see Novák and Grafarend (2006), only the latter two mass components are considered in this study. The internal mass density anomaly effects are namely due to the ocean mass density contrast and mass density jump from crust to mantle at the Moho. Effects of minor importance include mass density contrasts within sediments and crustal layers.

Once the spherical harmonic coefficients V_{nm} of the gravitational potential generated by a particular Earth’s mass component are estimated, see Eq. (12), respective gravitational gradients can easily be synthesized through Eqs. (14) and (16). These gradients can be used for reducing/stripping the disturbing gravitational gradients of Eq. (23) resulting in residual (corrected and stripped) gravitational gradients

$$\delta\Gamma^r(r, \Omega) = \delta\Gamma(r, \Omega) - \sum_k \Gamma^k(r, \Omega), \tag{24}$$

with the summation index k representing the k -th mass density component. Gravitational gradients Γ^r are generated by homogenous topographic masses (t). Remaining gravitational gradients are due to mass density contrasts (with respect to the mean crustal density of

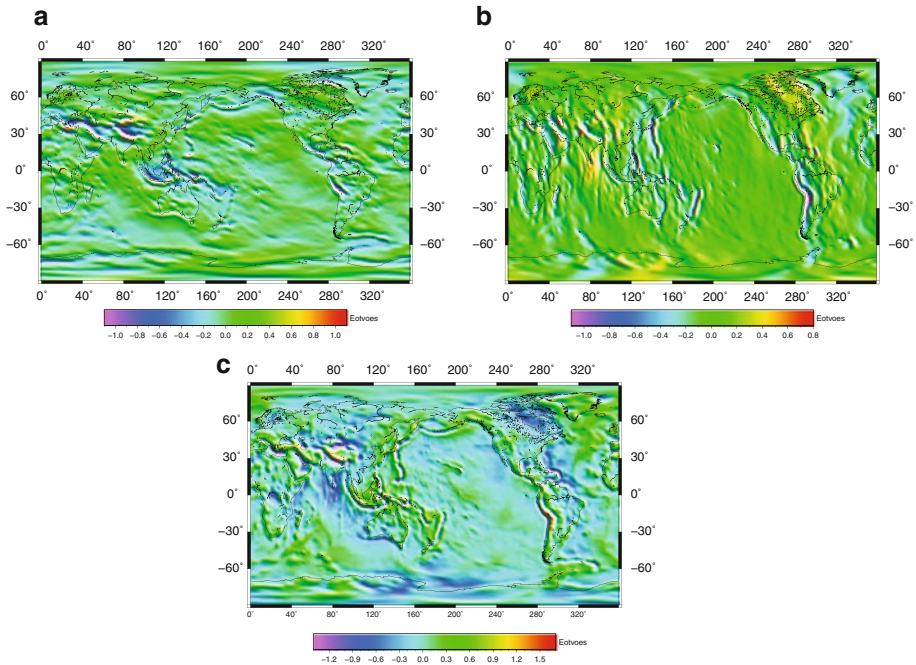


Fig. 3 GOCO-03S/GRS80 disturbing gravitational gradients (from top $\delta\Gamma_{xx}$, $\delta\Gamma_{yy}$ and $\delta\Gamma_{zz}$)

$2,670 \text{ kg m}^{-3}$, see, e.g., Hinze 2003) within bathymetry (*b*), continental ice sheets (*i*), sediments (*s*) and crustal layers (*c*). Gravitational gradients were computed at the equiangular 0.5 arc-deg global grid at the elevation of 250 km that approximately corresponds to orbital elevation of the GOCE satellite. However, the spectral content of the computed values is limited by degree/order 90.

Topography-corrected disturbing gravitational gradients—diagonal entries of the Marussi tensor in LNOF—are plotted in Fig. 4. Residual gravitational gradients—diagonal entries of the Marussi tensor in LNOF—after the progressive application of the gravitational gradients generated by the k -th mass components are plotted in Figs. 5, 6, 7. Applying the topographic and bathymetric gradient corrections, see Fig. 5, distinct features of topography (large mountain ranges) as well as of the ocean bottom (large trenches) are clearly visible. Ice sheet gradient corrections removed large local signals over Greenland and Antarctica namely in the $\delta\Gamma_{zz}$ component shown in Fig. 6. Corrections due to sediments are relatively small and do not change significantly the plots; thus, these reduced fields are not shown herein. In contrary, crust-generated gravitational gradients change significantly global maps, see Fig. 7. Although some of the large effects are compensated by the last correction (such as those over the Himalayas and the Andes), there are still many areas with large effects not sufficiently compensated (namely along coastlines).

As seen in Fig. 7, the maximum spatial variations in the gravitational gradients correspond with the areas of the significant changes in the lithospheric structure. These features comprise, for instance, margins between the oceanic and continental crustal structures, borders between significant orogens and basins, and structures of the oceanic lithosphere with pronounced boundaries between the mid-oceanic ridges (i.e., divergent

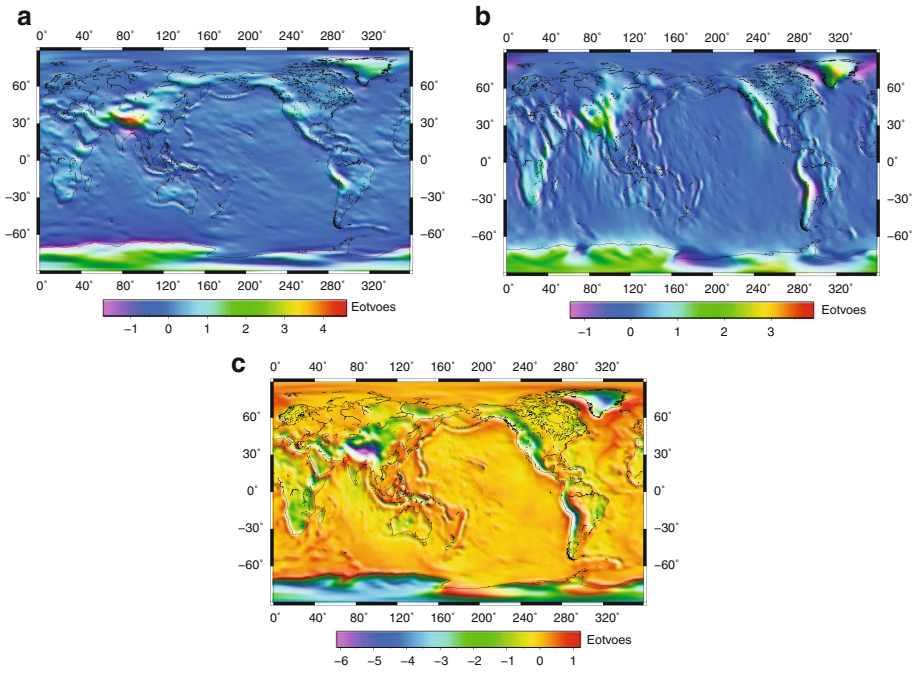


Fig. 4 Disturbing gravitational gradients reduced for topography

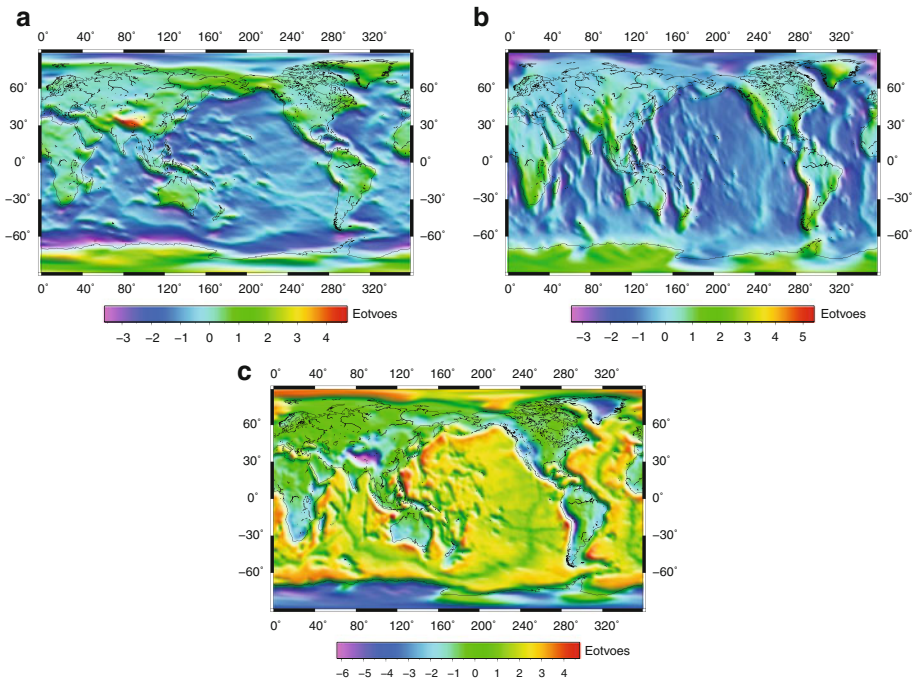


Fig. 5 Disturbing gravitational gradients reduced for topography and bathymetry

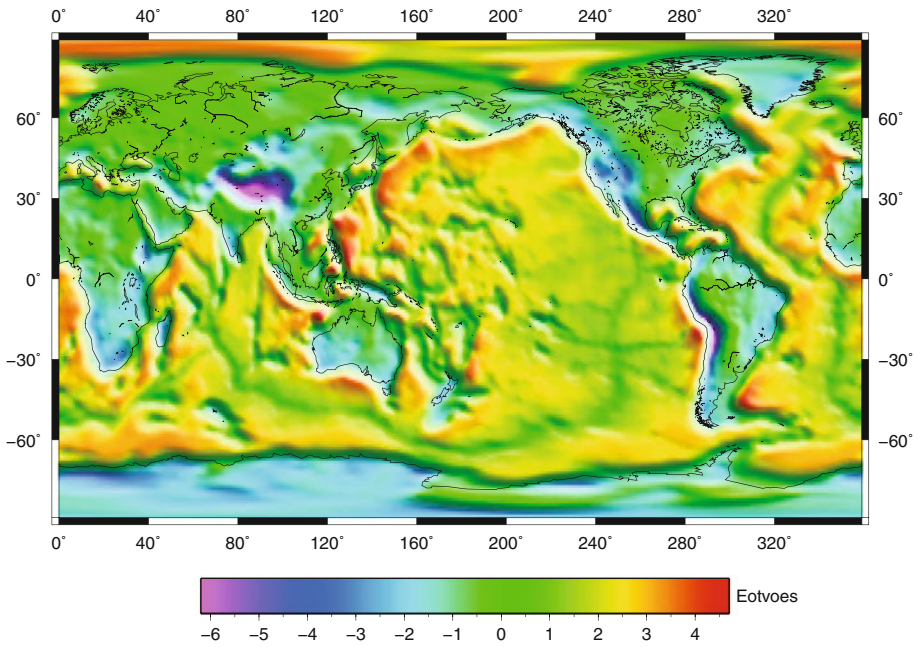


Fig. 6 Disturbing gravitational gradient $\delta\Gamma_{zz}$ reduced for topography, bathymetry and ice

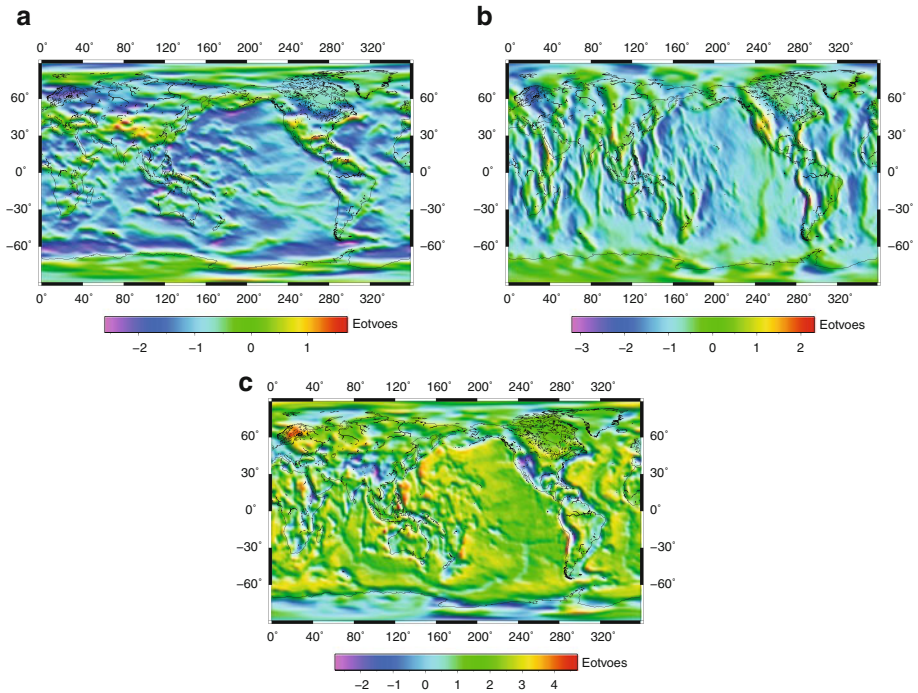


Fig. 7 Disturbing gravitational gradients reduced for all effects

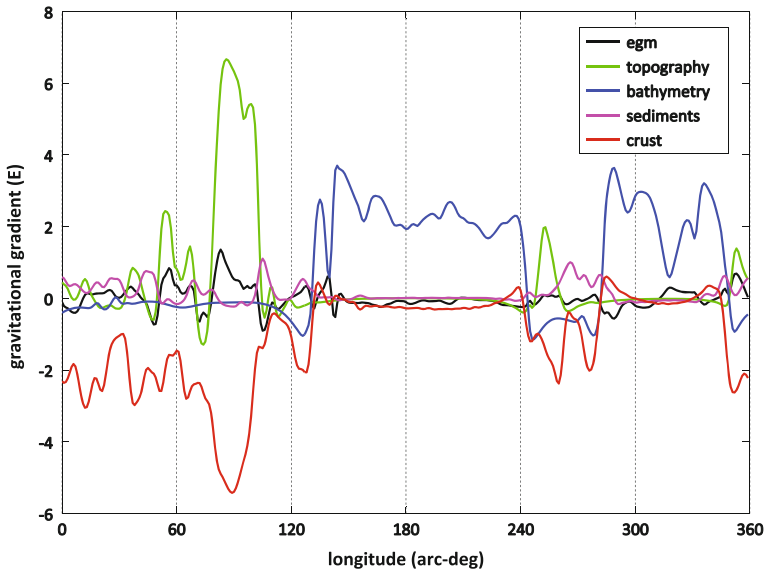


Fig. 8 Gravitational gradients Γ_{zz}^k ($k = t, b, s, c$) along the 30 arc-deg parallel north

tectonic plate boundaries) and oceanic subduction zones. Another oceanic lithosphere structures, which can easily be recognized, are contrasts between oceanic sedimentary basins and locations of hot spots. Over continental regions, boundaries between different geological structures are enhanced.

In Fig. 8, values of gravitational gradients $\delta\Gamma_{zz}$ evaluated along the parallel of 30 arc-deg north with regular spacing of 0.5 arc-deg are shown. The parallel crosses some interesting geographic areas including the Himalayas (within the longitude of ~ 70 to 110 arc-deg), Japanese Trench (~ 140 arc-deg), Pacific Ocean (~ 140 to 240 arc-deg), North American continent (~ 240 to 280 arc-deg) and Atlantic Ocean (~ 280 to 340 arc-deg). The lack of compensation of the four major components (topography, bathymetry, sediments and crust) is clearly visible namely over oceanic areas where large values of bathymetry-generated gravitational gradient remain uncompensated by mass densities within the crust.

Statistical values of the gravitational gradients after consecutive applications of particular effects can be found in Table 1. The sequential application of various gravitational gradient corrections to observed data resulted in larger magnitudes of corrected/stripped gravitational gradients. The largest range is achieved by applying the combined topographic and bathymetric gradient corrections (up to 10 E for Γ_{zz}). Their magnitudes decreased again after the crust-generated gradients were applied. Still, the range of gravitational gradients corrected for all effects is approximately twice as large as that of the disturbing gravitational gradients.

The residual gravitational gradients correspond to unmodeled mass density variations within static atmosphere, topography, continental ice, bathymetry, sediments and crust layers as well as to inhomogeneous mass density structures within the lithosphere mantle and possibly also within the deeper mantle. As such, they could be used for constraining the mass densities taking into account both their spatial and spectral properties. The GOCE gravitational gradients improved significantly the information about the static Earth's gravitational field—namely, the accuracy of EGMs at the medium spectrum

Table 1 Statistics of GOCO-03S/GRS80 disturbing gravitational gradients (g) reduced for topography (t), bathymetry (b), ice (i), sediments (s) and crust (c); all values are in Eötvös

Option	Gradient	Min	Max	Mean	Sigma
g	$\delta\Gamma_{xx}$	-1.107	1.140	0.000	0.138
$g - t$		-1.700	4.535	0.091	0.540
$g - t - b$		-3.602	4.651	-0.373	1.105
$g - b - t - i$		-3.307	4.652	-0.398	0.958
$g - b - t - i - s$		-3.360	4.371	-0.347	0.961
$g - b - t - i - s - c$		-2.559	1.684	-0.824	0.556
g	$\delta\Gamma_{yy}$	-1.118	0.789	0.004	0.142
$g - t$		-1.215	3.815	0.184	0.537
$g - t - b$		-3.387	5.347	-0.216	1.076
$g - t - b - i$		-3.075	5.340	-0.304	0.932
$g - b - t - i - s$		-3.174	5.472	-0.248	0.939
$g - b - t - i - s - c$		-3.142	2.256	-0.754	0.523
g	$\delta\Gamma_{zz}$	-1.403	1.623	-0.004	0.240
$g - t$		-6.089	1.158	-0.276	0.957
$g - t - b$		-6.142	4.646	0.589	1.934
$g - t - b - i$		-6.140	4.647	0.702	1.665
$g - b - t - i - s$		-6.127	4.578	0.595	1.167
$g - b - t - i - s - c$		-2.726	4.628	1.570	0.938

(approximately between degrees 70 and 200 of spherical harmonics) largely increased. The most significant improvement was achieved especially over the continental regions where low-quality and/or resolution terrestrial or airborne gravity data were only available. For geophysical studies, the inversion of EGM-based gravitational gradients should lead to improved interpretation of the Earth's inner density structure (particularly of shallow mass density structures within the lithosphere) due to the fact that the gravitational gradients have a more localized character compared to gravity or potential quantities.

For a specific gravitational potential represented by a set of spherical harmonic coefficients, its power spectrum (so-called degree variances) can be computed by generalization of Parseval's theorem (van Gelderen and Koop 1997)

$$\sigma_n(V) = \sum_{m=-n}^n V_{nm}^2. \quad (25)$$

These values can be used to study the spectral characteristics of harmonic functions in general. Looking at the power spectra of the different signal components—degree variances computed from respective potential coefficients, see Fig. 9—the following conclusions can be drawn: 1—power spectra of topography (mean topographic density), bathymetry and crust (mass density contrast) exceeds that of EGM (over degrees 2–90); 2—power spectrum of the sediments is below that of EGM (over degrees 2–90); and 3—ice spectrum attenuates quickly with increasing degrees due to a geographically limited ice sheets.

Power spectra of reduced gravitational gradients are plotted in Fig. 10. Respective signals after the application of corrections due to ice sheets and sediments are not included in the figure as they do not change significantly with respect to power spectra (signal

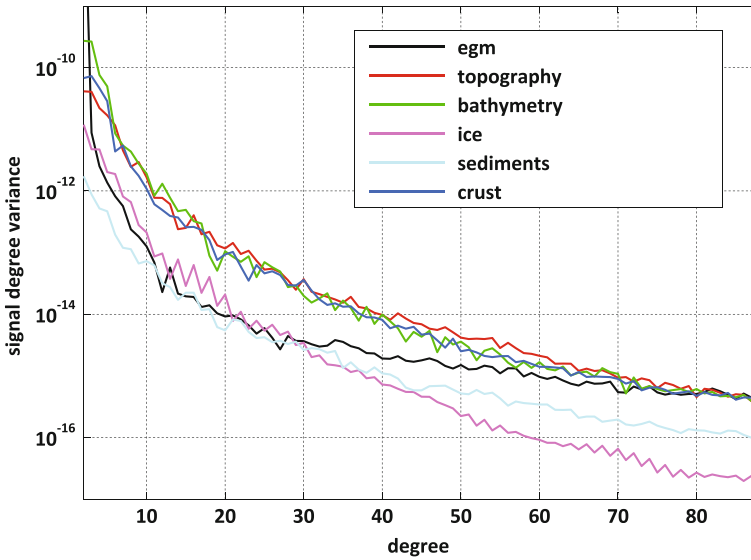


Fig. 9 Power spectra (degree variances) of the signal components

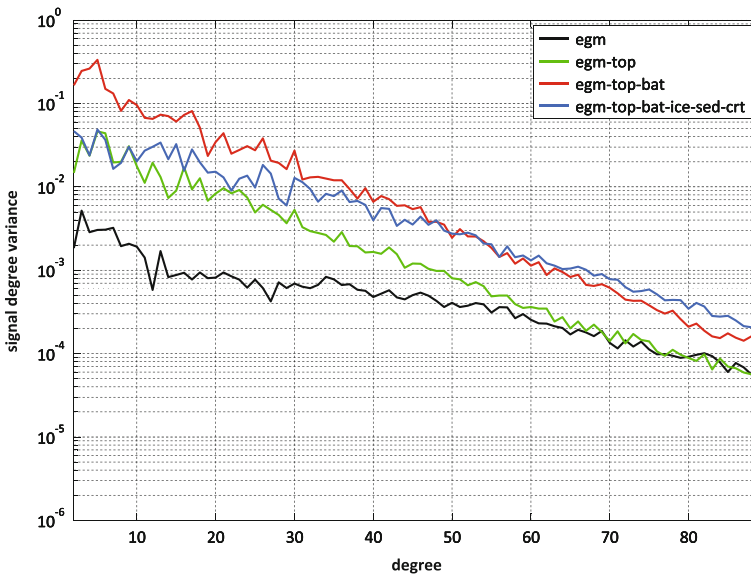


Fig. 10 Power spectra (degree variances) of the reduced gravitational gradients

degree variances). The power spectra of the computed gravitational gradients confirm the lack of compensation namely in the low degree band of spherical harmonic degrees.

Additionally, the degree correlations (correlation coefficients) of two sets of harmonic coefficients

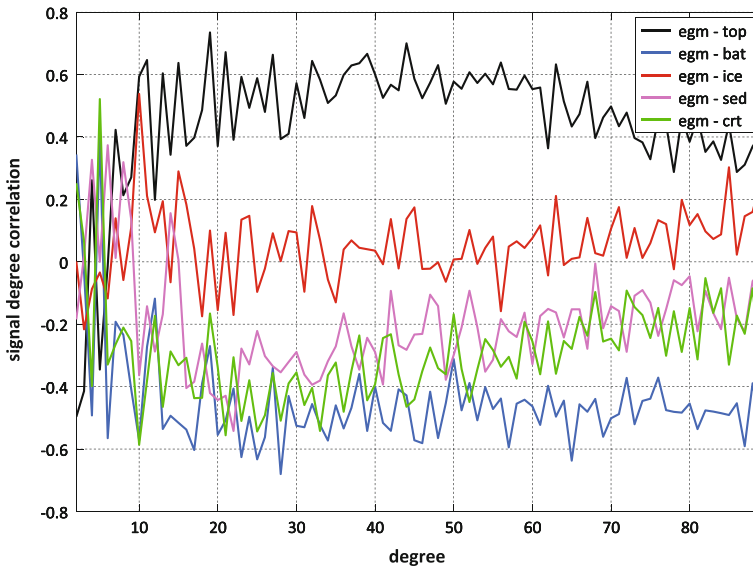


Fig. 11 Correlation spectra of the signal components

$$\rho_n(V^i, V^j) = [\sigma_n(V^i)\sigma_n(V^j)]^{-0.5} \sum_{m=0}^n V_{nm}^i V_{nm}^j, \quad (26)$$

can be used to investigate the degree-dependent relationship of two signal components V^i and V^j . Values of the correlation coefficients for the signal components discussed in this article are plotted in Fig. 11. The degree correlations for the pairs egm-topography and egm-bathymetry were presented and discussed, e.g., in Novák (2010). Other combinations show relatively small values of the correlation coefficients (over the plotted degree band 2–90). For the combination egm-ice, they correspond to strictly localized and geographically small areas covered by continental ice sheets. Remaining combinations (egm-sediments and egm-crust) have negative correlation coefficients with extreme values at the level of -0.6 over degrees 10–20 and decreasing to the level of -0.2 toward degree 90 reflecting the poor spatial resolution of the CRUST2.0 model.

6 Conclusions

Spectral forward modeling of gravitational gradients was applied for the derivation of global maps of the corrected/stripped gravitational gradients. The spectral formulas were successfully verified through an independent method represented by the discrete Newtonian integration. Respective corrections to observed gravitational gradients are represented by gravitational gradients generated by topographic masses of mean topographic mass density, and by mass density contrasts within oceans, continental ice sheets, sediments and crust layers. Values of the combined gravitational gradients generated by topography, bathymetry and continental ice were compared to their counterparts independently derived from the KIT model. Maximum relative differences reach 1 % of the individual gradient components. Individual gradient corrections were gradually applied to GOCE-based gravitational gradients reduced for the effect of the normal gravitational field generated by

the GRS-80 reference ellipsoid. Global spatial maps of corrected/stripped gravitational gradients then revealed geographic locations with the lack of compensation due to data or model deficiencies.

Spectral characteristics of the signal components represented in this study by degree variances and degree correlations indicate potential applications of the gravitational gradients in studying spectral properties of the Earth's gravity field, eventually for the validation of its spectral models routinely produced by geodesy. However, current crustal models have insufficient spatial resolutions to validate the entire range of applicable frequencies (measurement bandwidth) of GOCE observations. Power spectra of mean density topographic masses, ocean water (bathymetry) depth-dependent mass density contrasts and lateral crust mass density contrasts exceed that of the total field over the entire considered degree range 2–90 (limited by the CRUST2.0 spatial resolution) as Fig. 8 demonstrates. Reduced gravitational gradients have larger degree variances than the observed gravitational gradients (reduced for normal gravitational gradients). Finally, the degree correlations show relatively small dependencies between individual field components generated by the CRUST2.0 components and the total field (significant correlations are detected only for topography and bathymetry).

Future studies shall incorporate new CRUST models (more reliable and with higher spatial resolution) as well as the method of a geographically localized spectral analysis of gravitational parameters as their spectral properties vary largely with the location (spectral properties based on global data grids may not sufficiently be representative for studies of geophysically interesting and challenging areas). On the model side, new-generation GOCE-based Earth's gravitational models shall be released during 2013, which will take the advantage of large volumes of reprocessed GOCE gravitational gradients.

Residual gravitational gradients can be applied in various local geophysical studies such as modeling of margins between the oceanic and continental lithosphere, studies of subduction zones and hot spots due to the fact that the signature of the lithospheric structures has a strong localized character in the gravitational gradients than the corresponding signature in gravity data. However, the expected primary use of the gravitational gradients is in the context of studying shallow crustal structures as the resolving power of the gravitational gradients decreases fast with the spatial distance from gravitating masses. We also expect that more accurate gravimetric recovery of the crust–mantle density interface based on a combined inversion of isostatic gravitational data and the (isostatically compensated) gravitational gradients will be possible. However, a more detailed geophysical interpretation as well as the inversion of the gravitational gradients is out of the scope of this study.

Acknowledgments P. Novák was supported by the project 209/12/1929 of the Czech Science Foundation. We also acknowledge the research funding for foreign experts provided by the Chinese Ministry of Education.

Appendix 1: Gravitational Gradients in LNOF

First-order derivatives of the gravitational potential in the spherical coordinates read (with a derivative D and for the attenuation factor $\kappa = R/r \leq 1$)

$$V_r = -\frac{1}{R} \sum_{n,m} (n+1) \kappa^{n+2} V_{nm} Y_{nm}(\theta, \lambda), \quad (27)$$

$$V_\theta = \sum_{n,m} \kappa^{n+2} V_{n,m} D_\theta Y_{nm}(\theta, \lambda), \quad (28)$$

$$V_\lambda = \sum_{n,m} \kappa^{n+2} V_{nm} D_\lambda Y_{nm}(\theta, \lambda). \quad (29)$$

Second-order derivatives of the gravitational potential then read as follows:

$$V_{rr} = \frac{1}{R^2} \sum_{n,m} (n+1)(n+2) \kappa^{n+3} V_{n,m} Y_{nm}(\theta, \lambda), \quad (30)$$

$$V_{\theta\theta} = \sum_{n,m} \kappa^{n+3} V_{nm} D_\theta^2 Y_{nm}(\theta, \lambda), \quad (31)$$

$$V_{\lambda\lambda} = \sum_{n,m} \kappa^{n+3} V_{nm} D_\lambda^2 Y_{nm}(\theta, \lambda), \quad (32)$$

$$V_{r\theta} = -\frac{1}{R} \sum_{n,m} (n+1) \kappa^{n+3} V_{nm} D_\theta Y_{nm}(\theta, \lambda), \quad (33)$$

$$V_{r\lambda} = -\frac{1}{R} \sum_{n,m} (n+1) \kappa^{n+3} V_{nm} D_\lambda Y_{nm}(\theta, \lambda), \quad (34)$$

$$V_{\theta\lambda} = \sum_{n,m} \kappa^{n+3} V_{nm} D_{\theta\lambda}^2 Y_{nm}(\theta, \lambda). \quad (35)$$

Elements of the gradiometric tensor in LNOF are defined (Koop 1993) as

$$\Gamma_{xx} = \frac{1}{r} V_r + \frac{1}{r^2} V_{\theta\theta}, \quad (36)$$

$$\Gamma_{yy} = \frac{1}{r} V_r + \frac{1}{r^2 \tan \theta} V_\theta + \frac{1}{r^2 \sin^2 \theta} V_{\lambda\lambda}, \quad (37)$$

$$\Gamma_{zz} = V_{rr}, \quad (38)$$

$$\Gamma_{xy} = \frac{1}{r^2 \sin \theta} V_{\theta\lambda} - \frac{\cos \theta}{r^2 \sin^2 \theta} V_\lambda, \quad (39)$$

$$\Gamma_{xz} = \frac{1}{r^2}V_\theta - \frac{1}{r}V_{r\theta}, \quad (40)$$

$$\Gamma_{yz} = \frac{1}{r^2 \sin \theta}V_\lambda - \frac{1}{r \sin \theta}V_{r\lambda}. \quad (41)$$

Appendix 2: Radial Gravitational Gradient by Newtonian Integration

The radial gravitational gradient can be computed analytically by Eq. (22). The integrand I originates from the radial integration

$$I(r, \Omega, r_i, r_e, \Omega') = \int_{r_i(\Omega')}^{r_e(\Omega')} D_r^2 \mathcal{L}^{-1}(r, \Omega, \xi, \Omega') \xi^2 d\xi, \quad (42)$$

that can be evaluated as follows (Wild and Heck 2004):

$$I(r, \Omega, r_i, r_e, \Omega') = -\frac{r_e^3}{2\mathcal{L}_e} + \frac{r_i^3}{2\mathcal{L}_i} + r_e \mathcal{L}_e - r_i \mathcal{L}_i + \frac{r_e^3(r^2 - r_e^2)}{2\mathcal{L}_e^3} - \frac{r_i^3(r^2 - r_i^2)}{2\mathcal{L}_i^3} \\ + 3r \cos \psi (\mathcal{L}_e - \mathcal{L}_i) + r^2 (3 \cos^2 \psi - 1) \ln \left| \frac{\mathcal{L}_e + r_e - r \cos \psi}{\mathcal{L}_i + r_i - r \cos \psi} \right|. \quad (43)$$

The distance functions are defined as

$$\mathcal{L}_e = \sqrt{r^2 + r_e^2 - 2rr_e \cos \psi}, \quad (44)$$

and

$$\mathcal{L}_i = \sqrt{r^2 + r_i^2 - 2rr_i \cos \psi}. \quad (45)$$

Finally, ψ is the spherical distance between the two geocentric directions Ω and Ω' .

References

- Álvarez O, Gimenez M, Braitenberg C, Folguera A (2012) GOCE satellite derived gravity and gravity gradient corrected for topographic effect in the South Central Andes region. *Geophys J Int* 190(2):941–959
- Arfken G (1985) *Mathematical methods for physicists*, 3rd edn. Academic Press, Orlando
- Balmino G, Lambeck K, Kaula WM (1973) A spherical harmonic analysis of the Earth's topography. *J Geophys Res* 78(2):478–481
- Bassin C, Laske G, Masters G (2000) The current limits of resolution for surface wave tomography in North America. *EOS, Trans AGU* 81:F897
- Cohen CS, Smith DE (1985) LAGEOS Scientific results: introduction. *J Geophys Res Solid Earth*. 90(B11):92179220
- Ekhholm S (1996) A full coverage, high-resolution, topographic model of Greenland, computed from a variety of digital elevation data. *J Geophys Res* B10(21):961–972
- ESA, 2010, GOCE Level 2 Product Data Handbook. GO-MA-HPF-GS-0110. ESA Publication Division

- Floberghagen R, Fehrer M, Lamarre D, Muzi D, Frommknecht B, Steiger C, Piñeiro J, da Costa A (2011) Mission design, operation and exploitation of the gravity field and steady-state ocean circulation explorer (GOCE) mission. *J Geodesy* 85:749–758
- Gelderen van M, Koop R (1997) The use of degree variances in satellite gradiometry. *J Geodesy* 71:337–343
- Grombein T, Seitz S, Heck H (2012) Untersuchungen zur effizienten Berechnung topographischer Effekte auf den Gradiententensor am Fallbeispiel der Satellitengradiometriemission GOCE. KIT Scientific Reports 7547, Karlsruhe Institute of Technology, ISBN 978-3-86644-510-9
- Heiskanen WA, Moritz H (1967) *Physical geodesy*. Freeman and Co., San Francisco
- Hinze WJ (2003) Bouguer reduction density, why 2.67?. *Geophysics* 68(5):1559–1560
- Hirt C, Kuhn M, Featherstone WE, Göttl F (2012) Topographic/isostatic evaluation of new-generation GOCE gravity field models. *J Geophys Res B Solid Earth* 117(5):B05407
- Huang Q, Wiczorek MA (2012) Density and porosity of the lunar crust from gravity and topography. *J Geophys Res* 117:E05003
- Koop R (1993) *Global gravity field modelling using satellite gravity gradiometry*. Netherlands Geodetic Commission. Publications on Geodesy, 38, ISBN 90 6132 246 4
- Lachapelle G (1976) A spherical harmonic expansion of the isostatic reduction potential. *Bolletino di Geodesia e Scienze Affini* 35:281–299
- Lythe MB, Vaughan DG, BEDMAP consortium: (2001) BEDMAP; a new ice thickness and subglacial topographic model of Antarctica. *J Geophys Res B Solid Earth Planets* 106(6):11,335–11,351
- Mariani P, Braitenberg C, Ussami N (2013) Explaining the thick crust in Paran basin, Brazil, with satellite GOCE gravity observations. *J S Am Earth Sci* 45:209–223
- Mayer-Gürr T et al. (2012) The new combined satellite only model GOCO03s. Presentation at GGHS 2012, Venice, October 2012
- Moritz H (1990) The figure of the Earth. Wichmann H., Karlsruhe
- Moritz H (2000) Geodetic Reference System 1980. *J Geodesy* 74:128–162
- Novák P, Grafarend EW (2006) The effect of topographical and atmospheric masses on spaceborne gravimetric and gradiometric data. *Studia Geophysica et Geodetica* 50:549–582
- Novák P (2010) High resolution constituents of the Earth gravitational field. *Surveys Geophys* 31(1):1–21
- Novák P, Tenzer R, Eshagh M, Bagherbandi M (2013) Evaluation of gravitational gradients generated by Earth's crustal structures. *Comput Geosci* 51:22–33
- Pasyanos ME, Masters TG, Laske G, Ma Z (2011) Developing an updated global crust and upper mantle model using multiple data constraints. *Seism Res Lett* 82:310
- Pavlis NK, Factor JK, Holmes SA (2007) Terrain-related gravimetric quantities computed for the next EGM. In: Kiliçoğlu A, Forsberg R (eds) *Gravity field of the Earth. Proceedings of the 1st international symposium of the international gravity field service (IGFS)*, Harita Dergisi, Special Issue No. 18, General Command of Mapping, Ankara, Turkey
- Pavlis NK, Holmes SA, Kenyon SC, Factor JK (2012) The development and evaluation of the Earth Gravitational Model 2008 (EGM2008). *J Geophys Res* 117:B04406
- Phillips RJ, Lambeck K (1980) Gravity fields of the terrestrial planets: long-wavelength anomalies and tectonics. *Rev Geophys* 18(1):27–76
- Rapp RH (1981) The Earth's gravity field to degree and order 180 using Seasat altimeter data, terrestrial gravity data, and other data. Report of Dept. of Geodetic Science, The Ohio State University, Report No. 322, Columbus
- Reguzzoni M, Sampietro D (2012) Moho Estimation using GOCE data: a numerical simulation, In: *Proceedings Geodesy for Planet Earth, IAG Symposia Series 136(2):205–214*
- Rummel R (2005) Gravity and topography of Moon and planets. *Earth Moon Planets* 94:103–111
- Sünkel H (1986) *Global topographic-isostatic models in mathematical and numerical techniques in physical geodesy*. Lecture Notes in Earth Sciences, 418-462, Springer, Berlin
- Tapley BD, Bettadpur S, Watkins M, Reigber C (2004) The gravity recovery and climate experiment: Mission overview and early results. *Geophys Res Lett* 31(9):L09607
- Tenzer R, Hamayun Vajda P (2009) Global maps of the CRUST 2.0 crustal components stripped gravity disturbances. *J Geophys Res* 114:B05408
- Tenzer R, Novák P, Gladkikh V (2011) On the accuracy of the bathymetry-generated gravitational field quantities for a depth-dependent seawater density distribution. *Studia Geophysica et Geodaetica* 55:609–626
- Tenzer R, Novák P, Vajda P, Gladkikh V, Hamayun (2012) Spectral harmonic analysis and synthesis of Earth's crust gravity field. *Comput Geosci* 16(1):193–207
- Wessel P, Smith WHF (1991) Free software helps map and display data. *EOS Trans AGU* 72:441
- Wiczorek MA (2007) The gravity and topography of the terrestrial planets. *Treatise Geophys* 10:165–206
- Wild F, Heck B (2004) Effects of topographic and isostatic masses in satellite gravity gradiometry. 2nd International GOCE User Workshop, Frascati, March 8–10 2004